JOURNAL OF CATALYSIS 149, 70–80 (1994)

Design and Characterization by EXAFS, FTIR, and TEM of $Rh–Sn/SiO_2$ Catalysts Active for $NO–H_2$ Reaction

Keiichi Tomishige, Kiyotaka Asakura, and Yasuhiro Iwasawa[1]

Department of Chemistry, Graduate School of Science, The University of Tokyo, Hongo, Bunkyo-ku, Tokyo 113, Japan

Received December 7, 1993; revised March 16, 1994

$Rh–Sn/SiO_2$ catalysts, prepared by the selective reaction between Sn $(CH_3)_4$ and small Rh metallic particles supported on SiO_2, showed much higher catalytic activities for $NO–H_2$ reaction and NO dissociation than Rh/SiO_2 and coimpregnation $Rh–Sn/SiO_2$. In order to examine the important factors for the efficient catalysis of the $Rh–Sn/SiO_2$ catalysts, the samples were characterized by Sn *K*- and Rh *K*-edge EXAFS, FTIR, H_2 and CO adsorption, and TEM. For the $Rh–Sn/SiO_2$ catalysts ($Sn/Rh \geq 0.4$), the surface concentration of Sn to Rh was estimated to be $Sn_s/Rh_s = 3$, where a Rh atom is surrounded by six Sn atoms. According to the results of the Sn *K*-edge EXAFS analysis, the bond distance between a Sn atom and the nearest-neighbor atom in the first layer atoms was 0.270 nm, and the bond distance between a Sn atom and a metal atom in the second layer was 0.290 nm, suggesting a relaxation of the first bimetallic layer. A surface model structure of Rh–Sn particles on SiO_2 as a catalytically active bimetallic ensemble is discussed.

INTRODUCTION

In the $NO–H_2$ reaction on Rh/SiO_2, the rate-determining step has been reported to be NO dissociation assisted by adsorbed hydrogen atoms (1). A possible way to promote NO dissociation, and hence the catalytic activity of Rh/SiO_2, may be the addition of a second metal (*M*) as a promoter to form Rh–*M* alloys or intermetallics on SiO_2. The strategy for the design of bimetallic surface structures on SiO_2 active for $NO–H_2$ reaction in the present study was, first, to create bimetallic sites composed of Rh and an oxophilic metal which can interact wth the oxygen atom of NO molecule in order to weaken the N–O bond for its activation; second, to choose a suitable second metal with ready reducibility of its oxidized form (*M*–O bond) by hydrogen under mild reaction conditions so that the *M*–O bond which produced as a result of NO dissociation might easily be converted to a metallic state again; and, finally, to prepare an arrangement of surface atoms with a shorter $M \cdots O$ (NO) distance for easier interaction between NO oxygen and the adjacent *M* to Rh when NO adsorbs on an Rh atom.

The first and second ideas bring some limitations in the choice of the second metal. Many metals show advantageous interaction with oxygen. Table 1 lists the oxygen affinity of metals (2). The larger the pO value, the stronger the *M*–O bond becomes, and the reduction of the *M*–O bond is less likely to occur. The pO of the second metal (*M*) should be larger than that of Rh, by which oxygen atoms produced by NO dissociation can selectively be bound to the second metal atoms. Again the pO of the resultant *M*–O bond should be smaller than that of $H_2–H_2O$, preferably than that at $P_{H_2O}/P_{H_2} = 1$ in Table 1, so that the oxygen atom of the *M*–O bond can be transferred to H_2 to form H_2O. The third geometric requirement in the designing strategy may be achieved by a selecting as a second metal the one with the larger atom size compared to that of Rh. In fact, very recently the surface structure of a Pt–Sn single crystal has been characterized by LEED and ISS, which revealed that the Sn atoms are slightly protruded from the surface in the $\sqrt{3} \times \sqrt{3}$ ordered structure due to their larger atom size compared to Pt (3). If a similar arrangement is also achieved in the bimetallic particles of $Rh–Sn/SiO_2$ systems, the distance between the oxygen atom of NO molecule adsorbed on Rh atom and the adjacent second metal atom (Sn) may be shorter as compared to a flat surface, leading to an easier dissociation of the NO bond. In the present study, consequently, we chose Sn among the metals listed in Table 1 as the second metal to be added to Rh/SiO_2. The surface Sn atoms are reported to be stable up to 1000 K in the alloy single crystals (3), making the use of Sn as additive metal feasible.

While Sn metal has no significant catalytic activity by itself because it does not interact with H_2, hydrocarbons, CO, NO, and so on, Sn has been used as a promoter for SiO_2-supported transition metal catalysts to enhance their catalytic activity and selectivity. On $Pd–Sn/SiO_2$ and $Ni–Sn/SiO_2$ catalysts used for the dehydrogenation of cyclohexanone, cyclohexylamine, cyclohexane, and 2-propanol, the additive effect of Sn to Pd or Ni is suggested

[1] To whom correspondence should be addressed.

0021-9517/94 $6.00

TABLE 1

Oxygen Affinity of Metals

Oxide	pO^a
Rh_2O	4.2
TeO_2	7.2
Cu_2O	9.6
BiO	11.4
ReO_2	13.6
CoO	16.2
NiO	16.2
GeO_2	18.4
SnO_2	19.7
H_2–H_2O ($P_{H_2O}/P_{H_2} = 1$)	20.1
MoO_2	20.1
FeO	20.6
WO_2	21.2
K_2O	23.2
ZnO	25.8
H_2–H_2O ($P_{H_2O}/P_{H_2} = 10^{-3}$)	26.0

^{a} $pO = -\log P_{O_2} = -\Delta G_f^\circ/(2.3\,R)/1000$ for oxygen in equilibrium at 1000 K.

to be due to the dilution of the metal sites active for undesirable carbonaceous material deposition and due to the weakening of the adsorption bond by electronic modification (4, 5). These promoter effects are caused by the formation of alloys or intermetallic compounds. In addition, there is another additive effect owing to the interaction of Sn with the oxygen atoms of the reactants. In the CO oxidation reaction over Rh–Sn/SiO_2 catalysts, it was claimed that Sn enhanced the activation of oxygen molecules, decreased the self-poisoning by CO and/or O_2, and promoted the surface reaction between adsorbed oxygen and weakly adsorbed CO (6). In the selective hydrogenolysis of ethylacetate into ethanol over Rh–Sn/SiO_2, Ru–Sn/SiO_2, and Ni–Sn/SiO_2 catalysts which were prepared by the reaction between $Sn(C_4H_9)_4$ and oxidized Rh/SiO_2, Ru/SiO_2, and Ni/SiO_2, respectively, the selectivity to ethanol was much higher than the corresponding monometallic Rh/SiO_2, Ru/SiO_2, or Ni/SiO_2. It has been suggested that Sn atoms interacted with the oxygen lone pair of the carbonyl group of ethyl acetate (7–10).

There are many reports about the structure of Sn-containing alloy catalysts. The alloy phases such as Ni_3Sn_4, Ni_3Sn_2, and NiSn, and Pd_3Sn_2, PdSn, $PdSn_2$, and $PdSn_3$ have been detected to be present in Ni–Sn/SiO_2 and Pd–Sn/SiO_2, respectively, by means of XRD (4, 5). According to TEM observation, Pt–Sn particles in reduced Pt–Sn/SiO_2 form multiple phases containing PtSn, Pt_3Sn, and $PtSn_4$, and Rh–Sn particles in reduced Rh–Sn/SiO_2 form Rh_3Sn_2, $RhSn_2$ and $RhSn_4$ phases, where all particles are covered by thin layers of microcrystalline MSn_4 (M = Pt, Rh) (11). EXAFS, together with XRD measurements, indicates that alloy phases of Pt_3Sn, PtSn, and crystallites of Pt are present in Pt–Sn/SiO_2 (12). These results indicate that many bimetallic phases may be produced in Rh–Sn catalysts when the catalysts are prepared by a conventional coimpregnation method. To prepare better-defined Rh–Sn/SiO_2 catalysts the selective reaction of Sn $(CH_3)_4$ vapor with Rh metal particles supported on SiO_2 was employed in this study.

We have found that the obtained Rh–Sn/SiO_2 catalysts show much higher activity than Rh/SiO_2 and coimpregnation Rh–Sn/SiO_2 catalysts for the NO dissociation and the catalytic NO reduction by H_2 (13–15). The steady-state activity of the NO–H_2 reaction at 373 K increases with increasing the Sn content in the range of Sn/Rh $\leq$ 0.4, showing an S-shaped dependency, while the activity is nearly constant in the range of Sn/Rh $\geq$ 0.4 (13). At Sn/Rh = 0.4, the activity of Rh–Sn/SiO_2 becomes highest, and the turnover frequency (TOF) at 373 K is 75 times higher than that of Rh/SiO_2. In addition, on the Rh–Sn/SiO_2 catalysts, NO molecules were found to dissociate at ca. 200 K, whereas on Rh/SiO_2 little NO molecule dissociates in similar conditions. This kind of activation of the NO molecules is thought to be due to specific bimetallic ensemble structures. Typical results on the characterization of the first layer of Rh–Sn/SiO_2 by EXAFS have been reported (14). Very recently, the interaction of surface Sn atoms with the oxygen atoms of NO adsorbed on Rh atoms has also been observed (15, 16).

In this article, we report the detailed characterization of the Rh–Sn/SiO_2 catalysts by Sn K- and Rh K-edge EXAFS, TEM, FTIR, and CO and H_2 adsorption measurements in order to find structural features of bimetallic ensembles for the highly efficient catalysis.

EXPERIMENTAL

Preparation of Catalysts

SiO_2 (Aerosil 200 : 200 m^2/g) was immersed with a methanol solution of $RhCl_3 \cdot 3H_2O$ (Soekawa Chemical Co.), followed by drying at 373 K for 12 h and reduction with H_2 at 573 K for 1 h. The obtained Rh particles on SiO_2 were then reacted with given amount of Sn $(CH_3)_4$ (Soekawa Chemical Co.) vapor (<0.6 kPa) at 423 K for 15 min in a closed circulating system (dead volume: 200 cm^3). Figure 1 shows the CH_4 production during the reaction of $Sn(CH_3)_4$ with Rh/SiO_2 and SiO_2 alone. It is suggested from the results of the temperature-programmed reaction that more CH_4 molecules are produced by the reaction with Rh/SiO_2 than with SiO_2. In fact, the reactions of $Sn(CH_3)_4$ took place much more rapidly on Rh metal surfaces than with OH groups of SiO_2. Under the present conditions most of $Sn(CH_3)_4$ preferably reacted with Rh particles. The samples were finally reduced with H_2 at 573 K for 1 h, followed by evacuation *in situ* before use

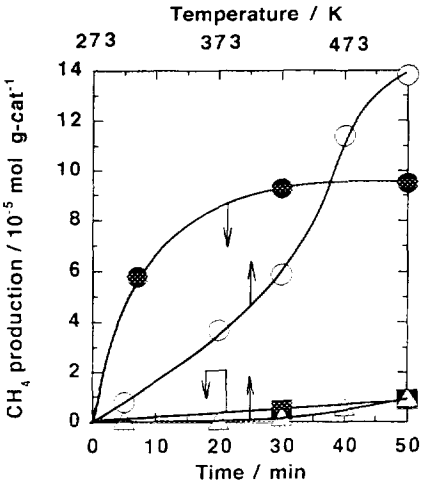

FIG. 1. The CH_4 production in the reaction of $Sn(CH_3)_4$ with Rh/SiO_2 and SiO_2: filled circle, reaction of $Sn(CH_3)_4$ (4.6×10^{-5} mol) with Rh/SiO_2 (1.0 g) at 423 K; filled square, reaction of $Sn(CH_3)_4$ (4.6×10^{-5} mol) with SiO_2 (1.0 g) at 423 K; open circle, temperature-programmed reaction of $Sn(CH_3)_4$ (1.7×10^{-5} mol) with Rh/SiO_2(0.2 g) (integrated amount); open triangle, temperature-programmed reaction of $Sn(CH_3)_4$ (1.7×10^{-5} mol) with SiO_2(0.2 g) (integrated amount); heating rate, 2 K/min.

as catalysts and also before each run. When $Sn(CH_3)_4$ reacted with Rh metal particles, two molecules of CH_4 per $Sn(CH_3)_4$ were evolved in gas phase and any other hydrocarbons were not observed. By further reduction at 573 K, two more CH_4 molecules were formed, leaving no residual carbon on the surface. The loading of Rh was controlled to be 1.0 wt%, while the Sn/Rh ratio was varied in the range 0–1. Coimpregnation $Rh–Sn/SiO_2$ (denoted as $Imp\text{-}Rh–Sn/SiO_2$) was prepared from a methanol solution of $RhCl_3 \cdot 3H_2O$ and $SnCl_2$. The pretreatment of these catalysts was performed in a similar way to the case of $Rh–Sn/SiO_2$.

Characterization of Catalysts

The amount of H_2 and CO adsorption on all catalysts was measured volumetrically in a closed circulating system (dead volume: 80 cm^3) under H_2 or CO of 13.3 kPa at 273 K. The amount of irreversible adsorption was estimated by subtracting the value obtained for reversible adsorption at the second adsorption experiment from the corresponding one from the first adsorption measurement. The catalysts were reduced by H_2 at 573 K for 1 h and evacuated for 1 h before the measurement.

X-ray absorption spectra at the Rh *K*- and Sn *K*-edges were measured at the BL-10B and 6B stations of the Photon Factory in the National Laboratory for High Energy Physics (Proposal No. 90003 and 92008) with a positron energy of 2.5 GeV and a maximum storage ring current of 350 mA. EXAFS data were collected in a transmission mode using ionization chambers filled with Ar for the I_0 signal and Kr for the I signal. X-rays from synchrotron radiation were monochromatized by a Si (311) channel cut crystal. The second harmonic is eliminated owing to the extinction rule of the Si (311), and the third and higher harmonics could be neglected owing to the low intensity of the photons with the corresponding energies emitted from the storage ring. The samples were treated in a closed circulating system and transferred to a glass cell with thin X-ray transparent glass windows for EXAFS spectra without contacting air. The EXAFS measurements were performed either at 298 or 70 K. The resulting data were analyzed by the EXAFS analysis program "EXAFS2N" (17). The analysis involves preedge extrapolation, background removal by a cubic spline method to extract EXAFS data, and Fourier transformation using a Hanning window function with 1/10 of the Fourier transform range. The typical ranges of Fourier transformation from the k space to the r space is 30–150 nm^{-1} for Rh *K*-edge EXAFS, and 30–120 nm^{-1} for Sn *K*-edge EXAFS spectra. The inverse Fourier transformation to the k space and the curve fitting were carried out to obtain detailed structural information.

We used the EXAFS formula based on a single scattering theory by the jth shell atom in the curve fitting analysis of EXAFS data,

$$\chi(k_j') = \sum_j N_j F(k_j') \exp(-2k_j'^2 \sigma_j^2) \sin(2k_j' R_j + \phi(k_j'))/k_j' R_j^2, \quad [1]$$

$$k_j' = (k_j^2 - 2m\Delta E_{0_j}/h^2)^{1/2}, \quad [2]$$

where k_j and ΔE_{0_j} are the photoelectron wavenumber and the difference between the origin of the photoelectron wave vector and that conventionally determined, respectively. $F(k_j')$ is the backscattering amplitude function, and $\phi_j(k_j')$ is the phase shift function. N_j, σ_j, and R_j are the coordination number, the Debye–Waller factor, and the interatomic distance, respectively. The fitting parameters are N_j, σ_j, R_j, and ΔE_{0_j}. The curve fitting is evaluated by an R factor (R_f) which is defined as

$$R_f = \int_{k_{min}}^{k_{max}} \left| k^3 \chi^{obs}(k) - k^3 \chi^{calc}(k) \right|^2 dk \Big/ \int_{k_{min}}^{k_{max}} \left| k^3 \chi^{obs}(k) \right|^2 dk. \quad [3]$$

Error bars for each parameter can be estimated by stepping each parameter, while optimizing the others parame-

TABLE 2

Curve Fitting Results for Sn *K*-Edge EXAFS Spectra of *β*-Sn

	C. N.[a]	R (nm)[b]	ΔE_0 (eV)[c]	σ(nm)[d]	R_f (%)[e]
Teo and	4.0	0.301	3.0	0.0087	4.7
Rh foil[f]	2.0	0.316	2.3	0.0094	
FEFF[g]	3.6	0.300	4.2	0.0082	3.0
	1.8	0.315	7.0	0.0100	
X-ray crystallographic	4.0	0.302			
analysis data	2.0	0.318			

Fourier transform range (30–140 nm^{-1}); Fourier filtering range (0.21–0.32 nm).

[a] Coordination number (coordination numbers were fixed in the curve fitting analysis).

[b] Bond distance.

[c] The energy difference between origins of the photoelectron wave vector.

[d] Debye–Waller factor.

[e] R factor, defined as $R_f = \int_{k_{min}}^{k_{max}} \left| k^3\chi^{obs}(k) - k^3\chi^{calc}(k) \right|^2 dk / \int_{k_{min}}^{k_{max}} \left| k^3\chi^{obs}(k) \right|^2 dk$.

[f] Curve fitting parameters: theoretical phase shift function (18) and empirical amplitude parameter extracted from Rh metal (C.N. = 12, R = 0.268 nm, σ = 0.0060 nm, ΔE_0 = 0.0 eV).

[g] Curve fitting parameters in FEFF was calculated by FEFF5.

ter, until R factor becomes two times as its minimum value. Since no good reference compound is available for Sn–Rh bonding, in the Sn *K*-edge EXAFS analysis we used the Rh backscattering amplitude derived from Rh foil for Sn–Rh because the atomic numbers of Rh and Sn only differ by 5. The phase shifts for this bonding were taken from the tabulated values (18). Validity of the theoretically derived parameters was checked by curve fitting analysis of Sn foil, as shown in Table 2. In addition, we performed the curve fitting analysis by FEFF5 (19, 20). The R factor of the curve fitting by FEFF is smaller than that by the parameter of Teo and Rh foil, but their fitting results are similar. In our case, the error bar may be estimated from the R factor and a little smaller error bars can be obtained by the FEFF analysis. The parameters (18–20) indicate that it was difficult to discriminate Sn–Rh and Sn–Sn bondings each other by the curve fitting analysis because of the similar values of the fitting parameters. In this article, curve fitting results show the average values of Sn–Rh and Sn–Sn bonding.

Transmission electron microscope photographs for determination of particles sizes were taken by means of JEM 2000EX (JEOL) equipment operated at 200 kV. After the reduction with H_2, the samples were stored under vacuum until the measurements were made. Samples were dispersed in tetrachloromethane by supersonic wave and put on Cu grids for the TEM observation under atmosphere. It took about 30 min of this handling before putting the sample into the TEM chamber, leading to oxidation of metal particle surfaces. However, the TEM images would be useful for comparing the photographs of bimetallic samples with those of monometallic samples to examine the distribution of particles of particles sizes and to check whether or not the distribution of particle size changes by Sn addition.

FTIR spectra were measured on a JASCO FT-IR 7000 spectrometer in an *in situ* IR cell which was combined in a closed circulating system. The Rh/SiO_2 sample was pressed into a self-supporting disk and put into a slit of the holder in the IR cell. The reduction of Rh/SiO_2 and the subsequent reaction with Sn $(CH_3)_4$ were conducted in the IR cell in the similar conditions above mentioned. IR absorption spectra were taken in a transmission mode and with 2-cm^{-1} resolution.

RESULTS

H_2 and CO Adsorption

Figure 2 shows the dependence of the steady-state activity of NO–H_2 reaction and H_2 and CO uptake on the amount of added Sn. The amount of adsorbed H_2 decreased steeply with increasing the Sn/Rh ratio and eventually to nearly zero in the range of Sn/Rh > 0.4. The CO uptake decreased almost linearly in the range of Sn/Rh < 0.4. Since H_2 and CO do not adsorb on Sn, the decrease in the amounts of H_2 and CO adsorbed is due to the decrease in the amount of Rh atoms at the surface of the bimetallic particles on SiO_2. The H_2 uptake decreased more drastically compared to that of CO adsorption because H_2 dissociation demands multisites (ensemble sites) of surface Rh atoms. The sharp break in activity for NO–H_2 reaction at 373 K corresponds to the sharp de-

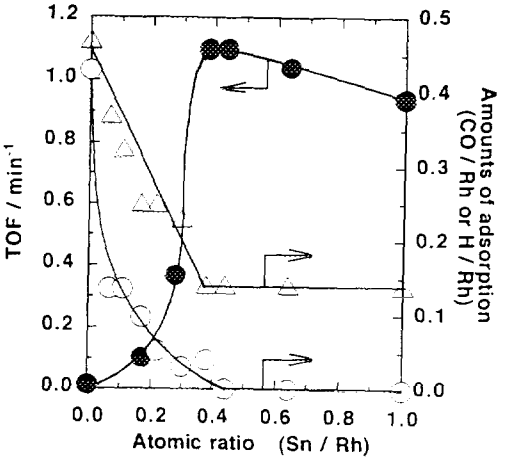

FIG. 2. The turnover frequency (product molecules per min per surface Rh atom) (TOF) for N_2 + N_2O formation in NO–H_2 reaction at 373 K on Rh-Sn/SiO_2 and the amount of H_2 and CO adsorbed on Rh–Sn/SiO_2 at 273 K: filled circle, TOF (NO : H_2 = 2.7 : 13.3 kPa); open circle, H/Rh (H_2 = 13.3 kPa); open triangle, CO/Rh (CO = 13.3 kPa).

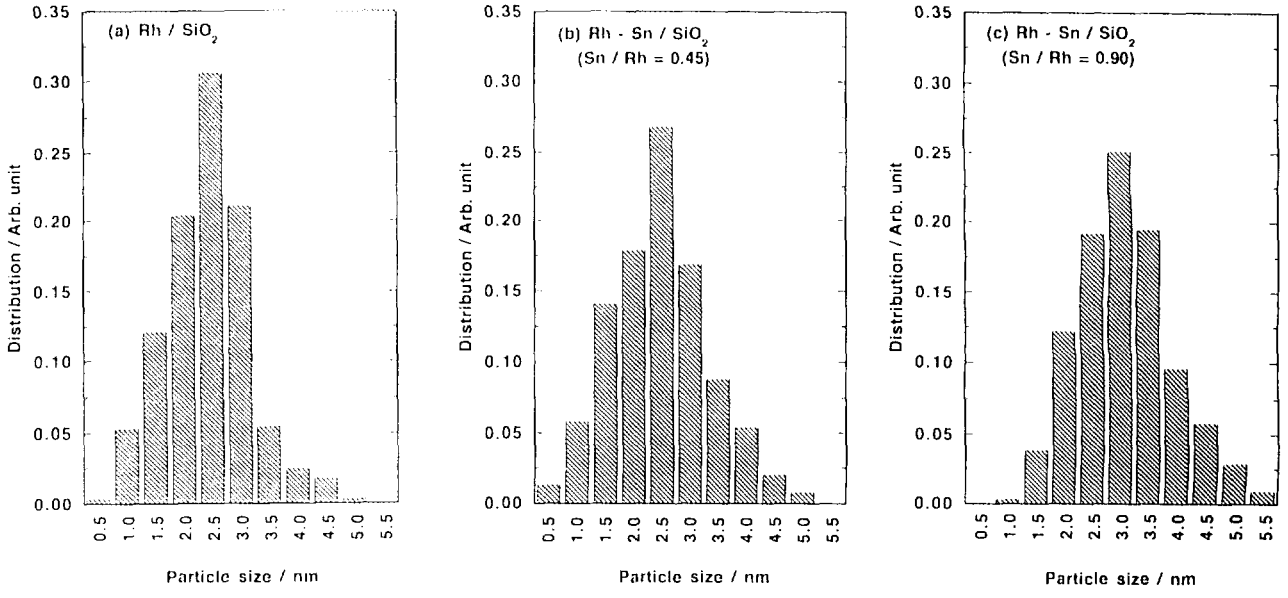

FIG. 3. The particle size distributions observed by TEM: (a) Rh/SiO_2; (b) $Rh–Sn/SiO_2$ (Sn/Rh = 0.45); (c) $Rh–Sn/SiO_2$ (Sn/Rh = 0.90).

crease and break in CO and H_2 uptakes, and perhaps to structural changes characterized hereinafter.

TEM Observation

Figure 3 shows the size distribution of the metal particles for Rh/SiO_2 and $Rh–Sn/SiO_2$(Sn/Rh = 0.45 and 0.90) samples obtained by TEM. The averaged particle sizes of Rh/SiO_2 and $Rh–Sn/SiO_2$ (Sn/Rh = 0.45) were found to be almost the same (2.5 ± 0.5 nm). The size distribution of metal particle is also similar to each other for both samples. On the other hand, the average particle size of $Rh–Sn/SiO_2$ (Sn/Rh = 0.90) was 3.0 ± 0.5 nm as shown in Fig. 3c. The TEM photographs were taken after exposure of the samples to air for about 30 min. From the Sn *K*-edge EXAFS for $Rh–Sn/SiO_2$ (Sn/Rh ≤ 0.4) Sn–Rh or –Sn bonds disappeared by exposing the sample to O_2, but on $Rh–Sn/SiO_2$ (Sn/Rh = 0.7) a part of Sn–Rh or –Sn bonds were sustained (14). Combined these results and the amounts of CO adsorption, in the range of Sn/Rh ≤ 0.4, Sn atoms are located at the surface of the metal particles where O_2 is accessible to Sn, whereas in the range of Sn/Rh > 0.4, a part of Sn atoms are located at the inside of the metal particles where O_2 is inaccessible. Under the condition of TEM observation, almost all the Sn atoms on $Rh–Sn/SiO_2$ (Sn/Rh = 0.45) were oxidized, while on $Rh–Sn/SiO_2$ (Sn/Rh = 0.90) about a half of Sn atoms remained nonoxidized at the inside of the particles. Thus the reason that the average particle size of $Rh–Sn/SiO_2$ (Sn/Rh = 0.45) was almost the same as that of Rh/SiO_2 may be due to the spreading of oxidized Sn formed during transfer of the sample to the TEM or due to an accidental coincidence with uncertainty of ±0.5 nm. In the case of $Rh–Sn/SiO_2$ (Sn/Rh = 0.90) the larger particle size (3.0 ± 0.5 nm) as compared to the size (2.5 ± 0.5 nm) for Rh/SiO_2 was observed. It would be valid to suggest that Rh metal particles do neither aggregate nor disperse by the addition of Sn from these results. Thus the decrease in the uptakes of H_2 and CO in Fig. 2 is not due to the change of the particle size.

IR Spectra of Adsorbed CO

Figure 4 shows the FTIR spectra obtained after CO adsorption on $Rh–Sn/SiO_2$ with various Sn/Rh ratios. The spectra were taken at 298 K and under CO of 13.3 kPa. On Rh/SiO_2, linear CO is observed at 2076 cm^{-1} and twofold bridge CO is observed at 1914 cm^{-1}. Besides them, geminal CO appears at 2100 and 2048 cm^{-1}. These assignments are based on the corresponding values reported in the literature (21–24). The geminal CO is known to be formed by the CO-induced oxidative disruption of Rh crystallites on Al_2O_3 and SiO_2 (25–27). It was reported that mobile metal carbonyl species are formed following CO adsorption and that these species diffuse across the surface, to become stabilized by the interaction with the support. The mobility of the species across the surface and the strength of the interaction may govern the rate at which particle disruption and agglomeration occur, and these are strongly influenced by the nature of the support surface (26, 27).

On $Rh–Sn/SiO_2$ (Sn/Rh = 0.08), the intensities of geminal and twofold bridge CO peaks decreased. At Sn/Rh = 0.31 these peaks disappeared, and only linear CO was

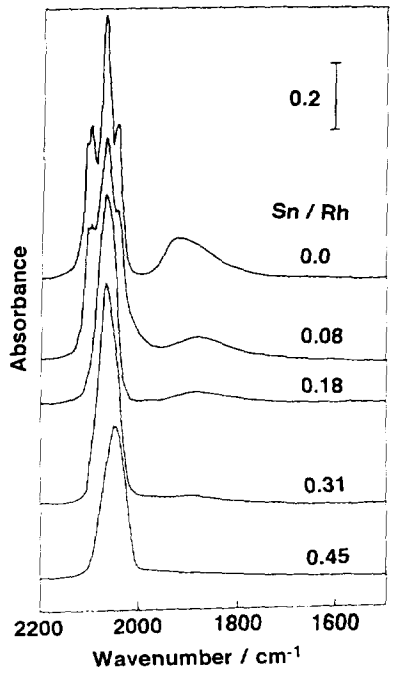

FIG. 4. FTIR spectra of CO adsorbed of Rh–Sn/SiO$_2$: pressure of CO, 13.3 kPa. Measurement temperature, 298 K; resolution, 2 cm^{-1}.

observed at 2064 cm^{-1}. This indicates that Rh atoms are isolated by the Sn atoms. Upon increasing Sn content, the frequency of linear CO peak shifted from 2076 to 2068, 2064, and 2050 cm^{-1} for Sn/Rh = 0.18, 0.31, and 0.45 respectively. The observed red shift of the linear CO peak induced by the more addition of Sn may be caused by the electronic modification of Rh sites and/or the decrease of dipole–dipole coupling of CO at surface. The large decrease in the amount of adsorbed CO in Fig. 2 would lead to certain red shifts of the CO peak due to the dipole–dipole decoupling, but, actually the small red shift of linear CO by 26 cm^{-1} on Rh–Sn/SiO$_2$ (Sn/Rh = 0.45) was only observed. Hence, the peak shift may be attributed mainly to the decrease of the dipole–dipole coupling while the electronic effect seems to be small.

EXAFS Analysis

Figure 5a shows the k^3-weighted Sn *K*-edge EXAFS oscillation for the reduced Rh–Sn/SiO$_2$ (Sn/Rh = 0.45) and its associated Fourier transform is shown in Fig. 5b, where the Fourier transforms for the catalysts with Sn/Rh = 0.17, 0.27, and 0.70 are also shown. The peak intensities for Sn–Rh or –Sn bonds in Fig. 5(b) did not largely depend on the amounts of Sn added. To obtain structural information of the Sn sites of the bimetallic particles, we performed at first a one-wave (Sn–Rh or –Sn) analysis for the EXAFS data using curve fitting technique. The Fourier transform of Fig. 5b was inversely Fourier-transformed to the *k*-space oscillation in Fig. 6a (solid line). The one-wave fitting curve shown by the dotted line in Fig. 6a does not well reproduce the experimental line in view of both the interval of oscillation and the feature of the envelope. The fitting result by one-wave analysis for the Rh–Sn/SiO$_2$ sample with Sn/Rh = 0.45 is shown in Table 3. The result for Sn/Rh = 0.27 was similar to that for Sn/Rh = 0.45. Next, we performed the two-wave (Sn – Rh or –Sn + Sn – Rh or – Sn) fitting analysis as shown in Fig. 6(b). The fitting was much improved as compared to the one-wave fitting. The best-fitting results for the three typical catalysts (Sn/Rh = 0.17, 0.27, and 0.45) are listed in Table 3. In the same Table are also listed the two-wave curve fitting results obtained with FEFF5. The relatively smaller coordination numbers are obtained because of the intrinsic loss of S_0^2 which is typically 0.9. We think that the results obtained by both theoretical analyses are essentially the same. There exist two different bond lengths with the values of 0.270 and 0.290 (±0.002) nm. The shorter bonds are the principal ones

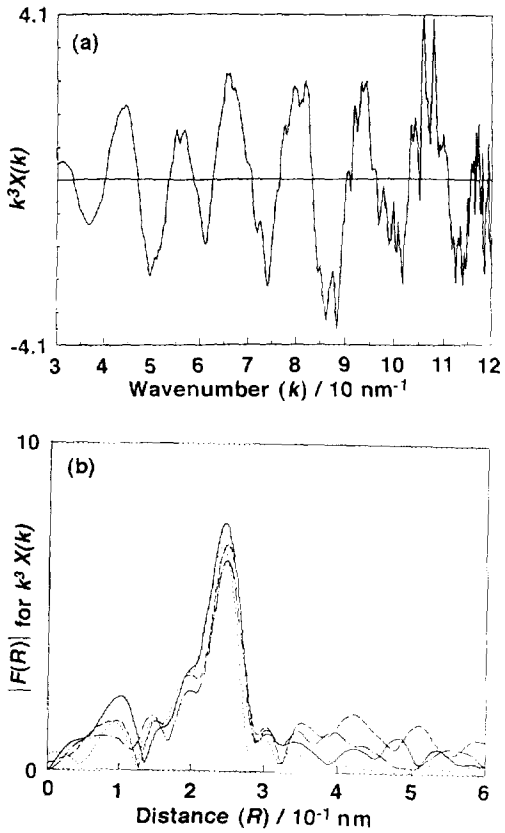

FIG. 5. Sn *K*-edge EXAFS spectra on Rh–Sn/SiO$_2$ after H$_2$ reduction at 573 K: (a) EXAFS oscillation of Rh–Sn/SiO$_2$ (Sn/Rh = 0.45); (b) Fourier transforms of Rh–Sn/SiO$_2$ for Sn/Rh = 0.17 (———), 0.27 (---), 0.45 (—·—), 0.70 (···). Fourier transform range, 30–120 nm^{-1}; measurement temperature, 298 K.

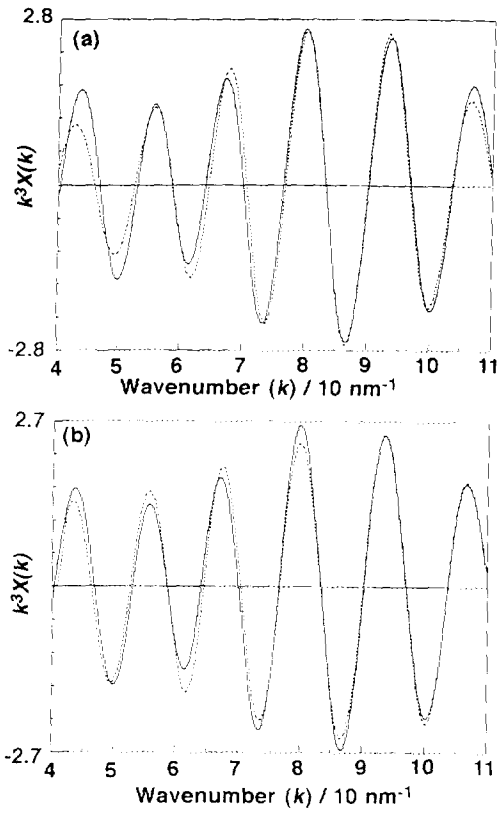

FIG. 6. Curve fitting of Sn K-edge EXAFS spectra for Rh–Sn/SiO_2 (Sn/Rh = 0.45): (a) curve fitting of Rh–Sn/SiO_2 by one wave (Sn–Rh or –Sn); (b) curve fitting of Rh–Sn/SiO_2 by two waves (Sn–Rh or –Sn + Sn–Rh or –Sn). Measurement temperature, 298 K; Fourier transform range, 30–120 nm^{-1}; Fourier filtering range, 0.15–0.32 nm; curve fitting parameter: theoretical phase shift function and empirical backscattering amplitude extracted from Rh metal measured at 70 K.

TABLE 3

Curve Fitting Results by One Wave and Two Waves of Sn–Rh or –Sn for Sn K-Edge EXAFS Spectra of the Reduced Rh–Sn/SiO_2

Sn/Rh	C. N.[a]	R(nm)[b]	ΔE_0(eV)[c]	σ(nm)[d]	R_f(%)[e]
0.17**	5.2 ± 2.0	0.268 ± 0.002	0.0 ± 4.0	0.0102 ± 0.0016	3.6
	1.7 ± 0.7	0.286 ± 0.002	7.9 ± 4.0	0.0115 ± 0.0016	
0.27**	6.4 ± 2.6	0.270 ± 0.002	4.4 ± 4.0	0.0109 ± 0.0016	4.0
	2.2 ± 0.9	0.289 ± 0.002	8.0 ± 4.5	0.0114 ± 0.0016	
0.45**	5.9 ± 2.4	0.270 ± 0.002	4.4 ± 4.0	0.0109 ± 0.0016	4.0
	2.6 ± 1.0	0.290 ± 0.002	6.3 ± 4.0	0.0114 ± 0.0016	
0.45**[f]	5.0 ± 2.0	0.268 ± 0.002	1.9 ± 3.0	0.0111 ± 0.0011	1.4
	2.4 ± 1.0	0.290 ± 0.002	−8.0 ± 3.0	0.0134 ± 0.0011	
0.45*	4.7 ± 2.1	0.269 ± 0.002	−0.8 ± 4.0	0.0111 ± 0.0016	5.7

Note. * One-wave fitting; **two-wave fitting. Fourier transform range (30–120 nm^{-1}); Fourier filtering range (0.15–0.32 nm); curve fitting parameters: theoretical phase shift function and empirical amplitude parameter extracted from Rh metal (C. N. = 12, R = 0.268 nm, σ = 0.0060 nm, ΔE_0 = 0.0 eV) except the FEFF analysis.

[a] Coordination number.

[b] Bond distance.

[c] The difference between origins of photoelectron wave vector.

[d] Debye–Waller factor.

[e] R factor, defined as $R_f = \int_{k_{min}}^{k_{max}} \left| k^3\chi^{obs}(k) - k^3\chi^{calc}(k) \right|^2 dk \Big/ \int_{k_{min}}^{k_{max}} \left| k^3\chi^{obs}(k) \right|^2 dk$.

[f] The FEFF curve fit by curve fitting parameters calculated by FEFF5.

and the longer bonds have the smaller coordination numbers. The 0.270-nm bond length is much smaller than the bond lengths of Sn–Sn bonds in α–Sn (0.284 nm) and β-Sn (0.302 nm). The obtained value is rather close to the bond length of Rh–Rh (0.268 nm) in the bulk metal. It means that all Sn atoms occupy the Rh metal lattice sites to form Rh–Sn alloy. It is well known that Sn forms substitutional alloys with some fcc metals.

Figure 7 shows the k^3-weighted Rh K-edge EXAFS oscillation for the Rh–Sn/SiO_2 (Sn/Rh = 0.45) catalysts (a), its associated Fourier transform (b), and a curve-fitting analysis (c). The oscillation (a) is similar to that for Rh metal EXAFS. We were able to obtain the best fitting by only using one-wave analysis of Rh–Rh (c). The intensity of the Rh–Rh peak at 0.2–0.3 nm in the Fourier transform decreased gradually by upon adding Sn as shown in Fig. 7b, suggesting a decrease in the coordination number of Rh–Rh bond. The best-fit results are listed in Table 4. Debye–Waller factors for Rh–Rh bonding were constant in the range of Sn/Rh < 0.3, and increased at Sn/Rh = 0.38 and 0.45. The decrease of the coordination number is thought to due to the fact that the Rh–Sn alloy phase has more static disorder than Rh metal particles, as indicated by the results of Sn K-edge EXAFS analysis shown in Table 3. This decrease in the peak intensity is not due to the decrease in the particle size as shown by TEM observation (Fig. 3). For the samples with Sn/Rh = 0.65 and 0.90, we were not able to obtain good fitting results.

TABLE 4

Curve Fitting Results for Rh K-Edge EXAFS Spectra of the Reduced Rh–Sn/SiO_2

Sn/Rh	C. N.[a]	R (nm)[b]	ΔE_0 (eV)[c]	σ(nm)[d]	R_f (%)[e]
0.0	11.0 ± 1.5	0.266 ± 0.001	10.5 ± 1.9	0.0075 ± 0.0004	1.2
0.09	9.7 ± 0.8	0.267 ± 0.001	3.0 ± 1.0	0.0074 ± 0.0002	0.6
0.19	8.2 ± 0.9	0.268 ± 0.001	0.7 ± 1.3	0.0074 ± 0.0003	0.9
0.27	7.8 ± 0.9	0.268 ± 0.001	0.5 ± 1.5	0.0076 ± 0.0003	1.1
0.38	6.2 ± 2.3	0.268 ± 0.001	−0.5 ± 4.0	0.0089 ± 0.0011	3.4
0.45	6.3 ± 0.9	0.269 ± 0.001	−1.8 ± 3.0	0.0090 ± 0.0009	2.8

Note. Fourier transform range (30–150 nm^{-1}); Fourier filtering range (0.15–0.30 nm); curve fitting parameters: empirical parameters extracted from Rh metal (C. N. = 12.0, R = 0.268 nm, ΔE_0 = 0.0 eV, σ = 0.0060 nm).

[a–e] See Table 3.

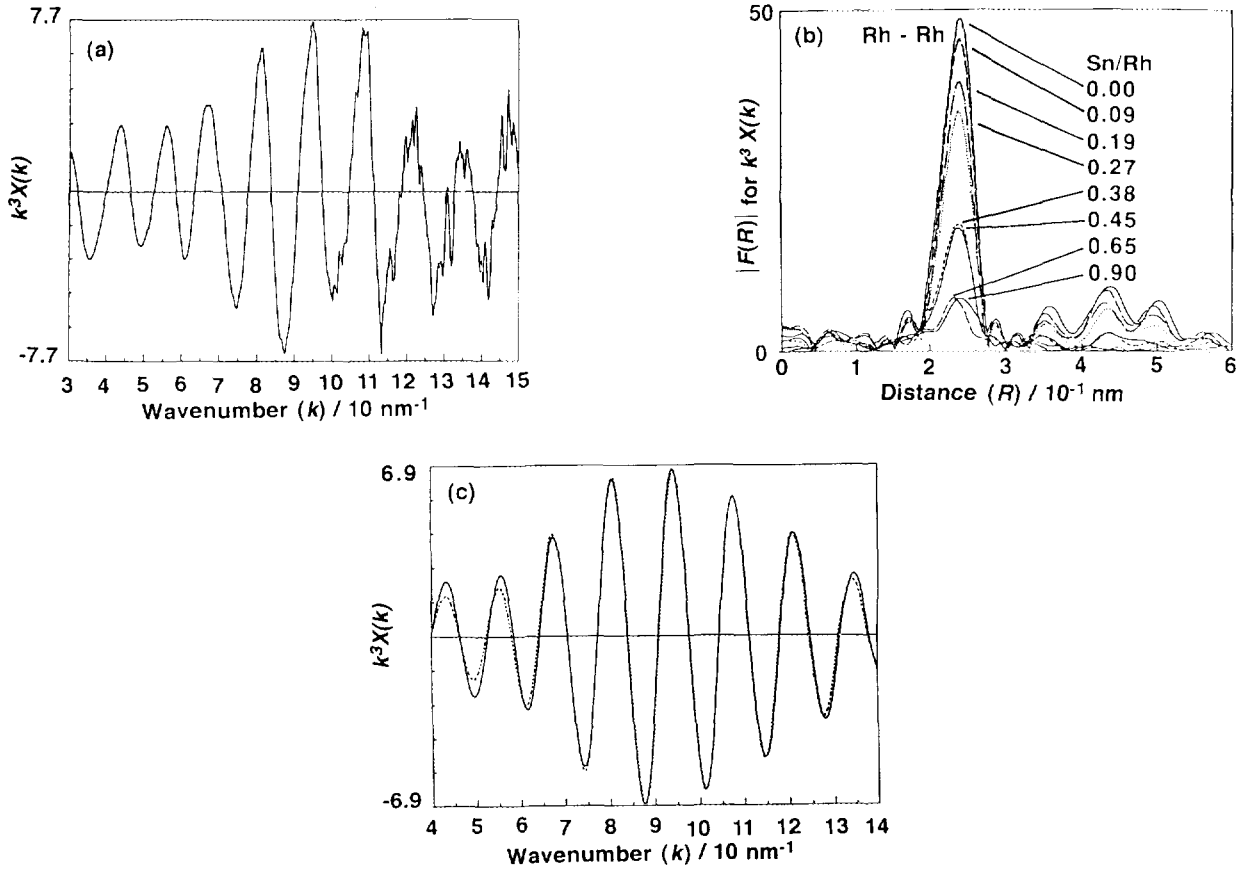

FIG. 7. Rh K-edge EXAFS spectra for Rh–Sn/SiO_2: (a) EXAFS oscillation of Rh–Sn/SiO_2 (Sn/Rh = 0.45); (b) Fourier transforms on Rh–Sn/SiO_2 with various Sn/Rh ratios; (c) curve fitting of Rh–Sn/SiO_2 (Sn/Rh = 0.45) by one wave (Rh–Rh). Measurement temperature, 298 K; Fourier transform range, 30–150 nm^{-1}; Fourier filtering range, 0.15–0.30 nm; curve fitting parameter: empirical phase shift and backscattering amplitude functions extracted from Rh foil measured at 70 K.

DISCUSSION

The catalytic activity of Rh–Sn/SiO_2 for NO–H_2 reaction shows a characteristic S-shaped dependency on the amount of Sn (Fig. 2). This type of dependency often indicates the formation of particular bimetallic ensemble sites at the surface of particles which are very active for NO dissociation and catalytic NO–H_2 reaction as compared to the monometallic Rh sites. The sharp break in activity at Sn/Rh = 0.4 corresponded to the sharp break in CO adsorption (Fig. 2) and also the discontinuous increase the Debye–Waller factor (Table 4). Therefore, it is important to estimate the surface Sn/Rh ratios and to determine the Rh–Sn bimetallic ensemble structures.

Estimation of Surface Composition of Rh–Sn Bimetallic Particles

Generally, it is not easy to estimate the surface composition of alloy catalysts because of the various possible location of the additive metal, for example, on the surface, in the bulk, or on the support. In the case of our Rh–Sn/SiO_2 (Sn/Rh $\leq$ 0.4) catalysts which were prepared by the selective reaction between given amounts of Sn $(CH_3)_4$ vapor and Rh particles on SiO_2, Sn atoms preferentially reacted with the surface of the Rh particles at 423 K as shown in Fig. 1. At 423 K only a few percent of $Sn(CH_3)_4$ vapor reacted with silanol groups in 30 min, showing a slow reaction with SiO_2 support. Similar results were recently reported by Nedez *et al.*, who also observed higher reactivities of SnR_4 (R: Et, *i*-Pr, and *n*-Bu) with SiO_2 (28). The reaction of Sn $(CH_3)_4$ vapor with Rh metal particles proceeded much more rapidly, where the reaction was completed with 5 min. In addition, it is possible to know the number of surface Rh atoms on Rh–Sn/SiO_2 by the amount of CO adsorbed. This is because on Rh–Sn/SiO_2 catalysts (Sn/Rh > 0.17) only linear CO was observed by FTIR in Fig. 4, and Sn atoms do not adsorb CO.

The amount of adsorbed CO decreased with an increase of Sn added. According to the TEM results shown in Fig. 3, the decrease in CO uptake is not due to the aggregation

to larger particles. The EXAFS data for the Rh–Sn/SiO_2 samples demonstrate that Sn is situated in a metallic state, showing Sn–Rh and/or Sn–Sn bonds. Sn atoms in the bimetallic particles with Sn/Rh = 0.3 are all accessible to oxygen and can form Sn–O bonds at 0.205 nm at 298 K (14). This phenomenon was also observed with all Rh–Sn/SiO_2 (Sn/Rh $\leq$ 0.4) samples. In contrast, the peak intensity of Sn–Rh or Sn–Sn bonds for the Imp-Rh–Sn/SiO_2 (Sn/Rh = 0.30) samples only decreased to about half of the original intensity when exposed to O_2 at 298 K, suggesting that about half of the Sn atoms in the Rh–Sn bimetallic particles prepared by a coimpregnation method are located inside the particles, even at Sn/Rh = 0.30. Furthermore for the Rh–Sn/SiO_2, in the composition range of Sn/Rh > 0.4 a part of Sn–Rh or –Sn bonds remained without oxidation with O_2. This indicates that an excess of Sn atoms intrude into Rh particles (14). The amount of CO adsorbed on the Rh–Sn/SiO_2 catalysts was constant in the composition range of Sn/Rh > 0.4, indicating that above this value, the surface becomes saturated with Sn atoms.

There are two possibilities for the location of the Sn atoms for samples in the composition range of Sn/Rh $\leq$ 0.4; simple adsorption on the Rh particle surface and bimetallic layer formation at the particle surface. Little change in the peak intensity of the Sn–Rh or –Sn bonds in the Fourier transform of the Sn *K*-edge EXAFS observed in the range Sn/Rh = 0.17–0.70 implies the incorporation of Sn to the first layer of the Rh particles surface rather than the adsorption on the Rh particles (Sn/Rh < 0.4), followed by the incorporation into the second layer and the bulk (Sn/Rh > 0.4), because Sn atoms in the Rh–Sn/SiO_2 catalysts with Sn/Rh = 0.70 are located at the surfaces accessible to O_2 and also in the bulk inaccessible to O_2. If Sn atoms at Sn/Rh $\leq$ 0.4 are simply adsorbed on the Rh particle surfaces, the peak intensity of the EXAFS Fourier transforms in Fig. 5b which reflects the number of metal atoms around a Sn atom would be more strongly varied upon increasing the Sn content from 0.17–0.27 to 0.45–0.70 for Sn/Rh ratios. Furthermore, the coordination number of the Rh–Rh bonds (Table 4) calculated from the EXAFS data of Fig. 7 decreased gradually and from the initial stage by Sn addition. This fact may exclude a simple adsorption of Sn atoms on the Rh surface. Thus we conclude that Sn atoms form the Sn–Rh bimetallic top-layer at the Rh particle surface in the composition range of Sn/Rh $\leq$ 0.4. A recent report on Sn/Cu(111), Ni(111), and Pt(111) which shows the $\sqrt{3} \times \sqrt{3}$ structure of stable surface alloys supports our conclusion (3).

On the basis of these results, we estimated the surface composition of Rh–Sn/SiO_2, assuming that (1) the morphology of metal particles is a sphere, (2) the surface of particles is fcc (111) as the most surfaces of fcc metal, and (3) the size of Rh metal particles on which Sn atoms form the surface alloys is 2.5 nm (TEM). A 2.5-nm Rh metal particle has about 6.0×10^2 Rh atoms and the particle becomes a little bigger by surface alloying with Sn. The size of these alloy particles can be calculated through the relationship between the number of total atoms of the particle and its size (Eq. [4]). From the size of the alloy particle, it is possible to estimate the number of surface metal atoms (the sum of surface Rh and Sn atoms) using Eq. [5],

$$N_t = 0.74 \times (4/3 \cdot \pi R^3)/(4/3 \cdot \pi a^3), \quad [4]$$

$$N_s = (\pi/2\sqrt{3}) \times 4\pi (R - a)^2/(\pi a^2), \quad [5]$$

where N_t is the number of total metal atoms of the alloy particle, N_s is the number of surface metal atoms, R is the diameter of the alloy particle, and a is the diameter of Rh and Sn atom (=0.268 nm in EXAFS).

In Eqs. [4] and [5], 0.74 and $\pi/2\sqrt{3}$ are the fractions of occupation in volume and area, respectively. If the particles on SiO_2 are assumed to have a cubo-octahedron shape, the estimated ratio Sn_s/Rh_s should be smaller than that estimated for a sphere shape, but the difference would be about 20%. This would not require any essential change in the present discussion.

Since all Sn atoms are located at the surface layer of the alloy particles, the difference between the number of surface metal atoms and that of Sn atoms is equal to the number of surface Rh atoms. We calculated the number of surface Rh atoms and compared it with the experimental value of surface Rh atoms estimated from the amount of adsorbed CO assuming CO/surface Rh = 1. When Sn/Rh = 0.2, 0.3, and 0.4, the ratios of surface Sn atoms to surface Rh atoms were accordingly calculated to be 0.7, 1.4, and 2.9. These values correspond to the amounts of adsorbed CO of 0.28, 0.21, and 0.14 as CO/Rh. The observed values in Fig. 2 are 0.25, 0.23, and 0.14, respectively. The simulated values and the observed values are in good agreement in the composition range of Sn/Rh $\leq$ 0.4. In the range of Sn/Rh > 0.4, the amount of adsorbed CO was constant, indicating that the surface composition of these surfaces is the same as that of Sn/Rh = 0.4, where surface Sn concentration is regarded to be saturated. Thus the surface composition at saturation is suggested to be $Sn_s/Rh_s \approx 3$. The top view for the bimetallic surface layer is illustrated in Fig. 8, where a Rh atom is surrounded by six Sn atoms. This active ensemble structure for NO dissociation and catalytic NO–H_2 reaction seems to be formed at samples with Sn/Rh $\geq$ 0.2 as suggested from the results of Fig. 2. The surface composition at saturation is much larger than the saturation composition (Sn_s/M_s = 0.5 (M = Pt, Ni, and Cu) reported for

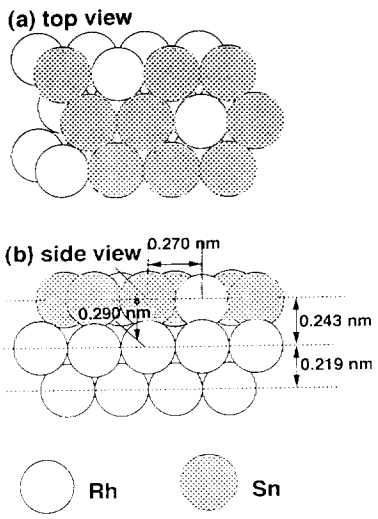

FIG. 8. A surface model structure of Rh–Sn/SiO_2 (Sn/Rh = 0.4) assuming that Rh–Sn bimetallic particles are spherical and have a fcc (111) surface: distance between Sn (first layer) and Rh (second layer) = 0.290 nm; atomic radius of Rh atom = 0.134 nm; atomic radius of Sn atom = 0.136 nm.

Sn/Pt(111), Ni(111), and Cu(111) (3, 29–31). In the case of the Sn/Pd system, c (2 × 2)-Sn/Pd(100) surface alloy with the Sn_s/Pd_s = 1 was observed (32). In the Sn/Ru system, ($\sqrt{3} \times \sqrt{3}$)-Sn/Ru(001) was observed at Sn_s/Ru_s = 2.0 (33). The saturation coverage for Sn may depend on the kind of the metal substrate and the orientation of its surface. It might also depend on the particle size.

Surface Structure of the Rh–Sn Bimetallic Particles

In the structure of the Rh–Sn bimetallic layer presented in Fig. 8a, the coordination number of Sn–Rh or –Sn bonds around the Sn atom in the first layer is expected to be 6 when the atom arrangement is fcc(111) plane. In addition, the Sn atoms should have a bonding with the three second-layer Rh atoms (Sn/Rh ≤ 0.4). However, the coordination number obtained by the one-wave curve-fitting analysis is 4.7 (±2.1), as shown in Table 3, which is much smaller than 9 (first and second layers). It is hardly thought that all the surface Sn atoms ($Sn_s/Rh_s \approx$ 3) are located at unsaturated sites like edges and corners because 2.5-nm metal particles cannot provide so many edge and corner sites for accommodation of 75% of the surface metal sites and Sn atoms are located at the sites to isolate Rh atoms as proved by IR of adsorbed CO. Thus the one-wave fitting analysis does not explain these observation. In fact, the one-wave fitting did not well reproduce the experimental curve in Fig. 6a. Recently the surface alloy structures of Sn/Cu(111), Sn/Ni(111), and Sn/Pt(111) surfaces which have a $\sqrt{3} \times \sqrt{3}$ LEED pattern have been reported (3). It has been demonstrated that the distance between the Sn atom of the first layer and the nearest-neighbor atoms of the second layer is longer than the distance between the Sn atom and the nearest-neighbor atoms in the first layer by 0.018–0.035 nm (3). Accordingly, we performed the curve-fitting of the Sn K-edge EXAFS by two-wave fitting analysis (Sn–Rh or –Sn + Sn–Rh or –Sn) as shown in Fig. 6b. The best fit results are shown in Table 3. The one-wave fitting results were much improved by the two-wave analysis, as indicated by the decrease of the residual factor from 5.7 to 4.0%. In the two-wave analysis, the longer Sn–Rh or –Sn bonds at 0.289 nm (Sn/Rh = 0.27)–0.290 nm (Sn/Rh = 0.45) were observed (Table 3). It may be of interest to compare this bond length with the bond length of Sn–Rh (0.2865 nm) in the intermetallic compounds RhSn and Rh_3Sn_2. The bond length of 0.290 nm (±0.002 nm) is attributable to the distance between the first-layer Sn atom and the second-layer Rh atoms. The determined coordination number of 2.6 (±1.0) presented in Table 3 is compatible with the value (3) for the geometric model discussed above. Then the coordination number around Sn atom within the first layer should be six for the fcc(111) plane in agreement with the value (5.9 ± 2.4) observed in this work (Table 3). The R_f values as a degree of the EXAFS curve fit were smaller with the FEFF5-based fit than for the Teo-based fit, as shown in Table 3, but the obtained results are similar. Based on the above discussion, we propose a surface structure shown in Fig. 8 for the Rh–Sn bimetallic particles on SiO_2. In the top layer a Rh atom is surrounded by six Sn atoms. As can be seen in Fig. 8, this arrangement produces a shallow hollow site around a Rh atom because the Sn atom size is a little larger than that of Rh. This was the expected ensemble structure in our design of these bimetallic catalysts. Furthermore, in the proposed surface structure the first layer is relaxed to elongate the separation between the first layer and the second layer by 0.024 nm as compared with the bulk separation as shown in Fig. 8b. No significant relaxation of the surface layer for the Rh(111) has been reported (33). The relaxation observed with the Rh–Sn bimetallic particles may be ascribed to the Sn–Rh separation observed with the stable intermetallic compounds (RhSn and Rh_3Sn_2).

The discussion was partly based on the assumption that the surface of Rh particles is mainly composed of Rh(111) face. However, if the particles take the cubo-octahedron geometry, the contribution of the (100) plane should also be taken into account in the structural analysis. In this case, the coordination number around a Sn atom for both the first and the second layer would be four, but the EXAFS analysis can not discriminate the minor contribution from the (100) plane. Fortunately, the above discus-

sion would be essentially valid also in the case of cubo-octahedron particles.

From the results obtained from the Rh *K*-edge EXAFS (Table 4), it was found that the coordination number of the Rh–Rh bonds decreased gradually by the addition of Sn. The decrease of the coordination number is not due to the decrease of the particle size as confirmed by TEM observation, it is apparent one. We cannot explain this large decrease in the coordination number of the Rh–Rh bond at present. Incorporation of Sn atoms to Rh lattice may give some distortion to the lattice. In fact, Sn–Rh or –Sn bonds had large Debye–Waller factors in Table 3.

CONCLUSIONS

(1) We designed the Rh-based bimetallic particles on SiO_2 for NO dissociation and catalytic NO–H_2 reaction on the idea of oxygen affinity of the additive metal and geometry of the ensemble structure.

(2) Sn was employed as the additive metal because the oxygen affinity of Sn is located between those of Rh and H_2, leading to ready dissociation of NO by chemical interaction of Sn with the oxygen atom of adsorbed NO and also to ready reduction of the resultant Sn–O bonds with H_2 to regenerate the original metallic state, and because the size of Sn atom is larger than that of Rh atom, leading to possible formation of a shallow hollow site on Rh which is a preferable geometry for NO dissociation.

(3) Rh–Sn/SiO_2 prepared by the reaction of $Sn(CH_3)_4$ and Rh metal particles supported on SiO_2 was very active for catalytic NO–H_2 reaction, where NO almost instantaneously dissociates, in contrast to the rate-determining NO dissociation step on Rh/SiO_2.

(4) We have characterized the surface structure of Rh–Sn bimetallic particles by Sn *K*-edge EXAFS and Rh *K*-edge EXAFS, FTIR, TEM, and measurement of the amount of H_2 and CO adsorption.

(5) Sn atoms in the bimetallic particles are located at the first layer of particles in the range of Sn/Rh $\leq$ 0.4. In the range of Sn/Rh $>$ 0.4, Sn atoms intrude into Rh metal particles.

(6) At saturation coverage of Sn the surface composition Sn_s/Rh_s is about three, where a Rh atom is surrounded by six Sn atoms.

(7) Sn–Rh or –Sn bonds in the first layer were observed at 0.270 nm. In addition, the longer bonding of Sn with the second-layer Rh atoms at 0.290 nm suggests that the relaxation of the first layer in the bimetallic particles. The distance between the first layer and the second layer is longer by 0.024 nm than the distance in the Rh fcc metal.

(8) This characterization of the Rh–Sn/SiO_2 catalysts may be useful for understanding promoter effects and important factors for the genesis of catalysis.

REFERENCES

1. Hecker, W. C., and Bell, A. T., *J. Catal.*, **92,** 247 (1985).
2. Reed, T. B., *in* "Free Energy of Formation of Binary Compounds," p. 67. MIT Press, Cambridge, MA, 1971.
3. Overbury, S. H., Ku, Y., *Phys. Rev. B* **46,** 7868 (1992).
4. Masai, M., Mori, K., Muramoto, H., Fujiwara, T., and Ohnaka, S., *J. Catal.* **38,** 128 (1975).
5. Masai, M., Honda, K., Kubota, A., Ohnaka, S., Nishikawa, Y., Nakahara, K., Kishi, K., and Ikeda, S., *J. Catal.* **50,** 419 (1977).
6. Nishiyama, S., Akemoto, M., Yamamoto, I., Tsuruya, S., and Masai, M., *J. Chem. Soc. Faraday Trans.* **88,** 3483 (1992).
7. Candy, J. P., Mansour, A. E., Ferretti, O. A., Mabilon, G., Bournonville, J. P., Basset, J. M., and Martino, G., *J. Catal.* **112,** 201 (1988).
8. Candy, J. P., Ferretti, O. A., Mabilon, G., Bournonville, J. P., Mansour, A. E., Basset, J. M., and Martino, G., *J. Catal.* **112,** 210 (1988).
9. Agnelli, M., Candy, J. P., Basset, J. M., Bournonville, J. P., and Ferretti, O. A., *J. Catal.* **121,** 236 (1990).
10. Basset, J. M., Candy, J. P., Louessard, P., Ferretti, O. A., and Bournonville, J. P., *Wiss. Z. TH Leuna-Merseburg* **32,** 657 (1990).
11. Chojnacki, T. P., and Schmidt, L. D., *J. Catal.* **129,** 473 (1991).
12. Meitzner, G., Via, G. H., Lytle, F. W., Fung, S. C., and Sinfelt, J. H., *J. Phys. Chem.* **92,** 2925, (1988).
13. Tomishige, K., Asakura, K., and Iwasawa, Y., *J. Chem. Soc. Chem. Commun.*, 184 (1993).
14. Tomishige, K., Asakura, K., and Iwasawa, Y., *Catal. Lett.* **20,** 15 (1993).
15. Tomishige, K., Asakura, K., and Iwasawa, Y., *Chem. Lett.* **235** (1994).
16. Tomishige, K., Asakura, K., and Iwasawa, Y., *Shokubai* **35,** 398 (1993).
17. Kosugi, N., and Kuroda, H., "Program EXAFS2N." University of Tokyo, 1987.
18. Teo, B. K., and Lee, P. A., *J. Am. Chem. Soc.* **101,** 2815 (1979).
19. Rehr, J. J., Leon, J. M., Zabinsky, S. I., and Albers, R. C., *J. Am. Chem. Soc.* **113,** 5135 (1991).
20. Leon, J. M., Rehr, J. J., Zabinsky, S. I., and Albers, R. C., *Phys. Rev. B* **44,** 4146 (1991).
21. Yang, A. Y., and Garland, C. W., *J. Phys. Chem.* **61,** 1505 (1957).
22. Yates, Jr., J. T., Duncan, T. M., Worley, S. D., and Vaughan, R. W., *J. Chem. Phys.* **70,** 1219 (1979).
23. Cavanagh, R. R., and Yates, Jr., J. T., *J. Chem. Phys.* **74,** 4150 (1981).
24. Solymosi, F., and Pasztor, M., *J. Am. Chem. Soc.* **89,** 4789 (1985).
25. van't Bilk, H. F. J., van Zon, J. B. A. D., Vis, J. C., Koningsberger, D. C., and Prins, R., *J. Am. Chem. Soc.* **107,** 3139 (1985).
26. Basu, P., Panayotov, D., and Yates, J. T. Jr., *J. Am. Chem. Soc.* **110,** 2074 (1988).
27. Anderson, J. A., Solymosi, F., *J. Chem. Soc. Faraday Trans.* **87,** 3435 (1991).
28. Nedez, C., Theolier, A., Lefefvre, F., Choplin, A., Basset, J. M., and Joly, J. F., *J. Am. Chem. Soc.* **115,** 722 (1993).
29. Paffett, M. T., and Windham, R. G., *Surf. Sci.* **208,** 34, (1989).
30. Paffett, M. T., Gebhard, S. C., Windham, R. G., and Koel, B. E., *J. Phys. Chem.* **94,** 6831 (1990).
31. Overbury, S. H., Mullins, D. R., Paffet, M. T., and Koel, B. E., *Surf. Sci.* **254,** 45 (1991).
32. Logan, A. D., and Paffett, M. T., *J. Catal.* **133,** 179 (1992).
33. Paffet, M. T., Logan, A. D., and Taylor, T. N., *J. Phys. Chem.* **97,** 690 (1993).
34. Hengrasmee, S., Mitchell, K. A. R., Watson, P. R., and White, S. J., *Can. J. Phys.* **58,** 200 (1980).